Communication

Hot-carrier extraction in nanowire-nanoantenna photovoltaic devices

I-Ju Chen, Steven Limpert, Wondwosen Metaferia, Claes Thelander, Lars Samuelson, Federico Capasso, Adam M. Burke, and Heiner Linke

Nano Lett., **Just Accepted Manuscript** • DOI: 10.1021/acs.nanolett.9b04873 • Publication Date (Web): 29 Apr 2020

Hot-carrier extraction in nanowire-nanoantenna photovoltaic devices

I-Ju Chen[1], Steven Limpert[1], Wondwosen Metaferia[1,2], Claes Thelander[1], Lars Samuelson[1], Federico Capasso[3], Adam M. Burke[1], Heiner Linke[1]

[1]NanoLund and Solid State Physics, Lund University, Box 118, SE-22100 Lund, Sweden

[2]National Renewable Energy Laboratory, Golden, CO 80401, United States

[3]Harvard John A. Paulson School of Engineering and Applied Sciences, Harvard University, Cambridge, Massachusetts 02138, USA

Abstract:

Nanowires bring new possibilities to the field of hot-carrier photovoltaics by providing flexibility in combining materials for band engineering and using nanophotonic effects to control light absorption. Previously, an open-circuit voltage beyond the Shockley-Queisser limit was demonstrated in hot-carrier devices based on InAs-InP-InAs nanowire heterostructures. However, in these first experiments, the location of light absorption, and therefore the precise mechanism of hot-carrier extraction, was uncontrolled. In this letter, we combine plasmonic nanoantennas with InAs-InP-InAs nanowire devices to enhance light absorption within a subwavelength region near an InP energy barrier that serves as an energy filter. From photon energy- and irradiance-dependent photocurrent and photovoltage measurements, we find that photocurrent generation is dominated by internal photoemission of non-thermalized hot electrons when the photoexcited electron energy is above the barrier, and by photo-thermionic emission when the energy is below the barrier. We estimate that an internal quantum efficiency up to 0.5–1.2% is achieved. Insights from this study provide guidelines to improve internal quantum efficiencies based on nanowire heterostructures.

Keywords: Hot electron, plasmonic, III-V nanowire heterostructure, photo-thermionic, internal photoemission, solar energy conversion

When semiconductors are excited by electromagnetic waves with photon energy $h\nu$ larger than the band gap, mobile electron-hole pairs are generated. As a result, there is an excess of electrons (holes) in the conduction (valence) band with nonequilibrium energy distributions. When $h\nu$ is sufficiently larger than the band gap, the photoexcited electrons and holes have higher kinetic energies than the lattice thermal energy, and they are thus called *hot carriers*, whether their energy distributions are thermalized or non-thermalized.[1]

The working principle of conventional solar cells and photodetectors are based on isothermal processes.[2] For example, in conventional p-n junction solar cells, carriers reach lattice temperature before they are separated, through fast thermalization and cooling processes while they drift across the depletion region. As a result, if $h\nu$ is significantly larger than the band gap, a big part of the photon energy is inherently lost as heat and the conversion efficiency in single-junction cells is bounded by the Shockley-Queisser limit[3,4]. Moreover, in p-i-n and Schottky photodiodes that collect quasi-equilibrium photo-carriers, the photocurrent signal recovery time can last as long as the carrier recombination lifetime[5] and limit their application in high-speed photodetection[6].

These limits to the performance of conventional solar cells and photodetectors can potentially be circumvented by extracting photo-generated hot carriers before they fully equilibrate with the lattice and even within carriers. Thermodynamic analysis has shown that a solar conversion efficiency larger than the Shockley-Queisser efficiency can be achieved by utilizing narrow band energy filters to separately extract hot electrons and holes that are equilibrated among themselves but not with the lattice[7–9]. Such narrow band energy filters have been realized based on double-barrier resonant tunneling semiconductor quantum wells[10,11] and in quantum dots embedded in nanowires[12]. In the latter, a near-ideal thermal-to-electric energy conversion efficiency was demonstrated.[12] A more common way to harness the kinetic energy of hot carriers is to extract them across an energy barrier, for example in semiconductor heterostructures, metal-semiconductor Schottky diode[13], and metal-insulator-metal structure[14,15]. An energy barrier embedded into a one-dimensional nanowire is expected to offer the best efficiency at maximum power.[16]

However, hot-carrier devices have been observed to have low internal quantum efficiencies for reasons including distribution of carriers at low-energy states, rapid carrier relaxation, carrier reflection by the barrier due to the lateral momentum conservation restriction, and cancellation by the reverse current[13–15,17–19]. Thus, a better control over and understanding of hot-carrier extraction is needed.

Semiconductor nanowires offer many desirable properties for hot-carrier devices compared to the planar structures typically used to date. First, due to strain relaxation, a larger selection of materials can be combined with high interface quality in nanowires than is possible in planar structures.[20] Therefore, the energy barrier and electron effective mass can potentially be tuned to optimize power conversion efficiency.[21,22] Secondly, carrier relaxation through carrier-phonon and carrier-carrier scattering can be less rapid in nanowires and nanowire heterostructures[23–25]. Finally, photonic effects in nanoscale semiconductors and metals offer unique design opportunities to concentrate light into deep-subwavelength volumes[26,27], and create hotter or higher concentration of hot carriers.

Recently, hot-carrier devices have been realized based on single nanowires with InAs-InP-InAs hetero-structures.[28,29] The InP energy barrier was used to extract hot electrons and reflect holes that were generated asymmetrically around the barrier due to photonic and plasmonic resonance effects. An open-circuit voltage exceeding the Shockley-Queisser limit of the low band gap InAs absorber was demonstrated, which provides convincing evidence that hot-carrier energy conversion contributed to the voltage generation in these devices.[28] In addition, a new photo-detection functionality with the polarity of the photo-current and photo-voltage changing with wavelengths was realized based on a similar structure, but with double InP barriers.[29] However, in these experiments the position and distribution of light absorption in the nanowire relative to the energy filter were not controlled, which makes it difficult to evaluate and optimize the hot-carrier extraction, a pre-requisite to improving internal quantum efficiency.

Here, we address these challenges by using plasmonic nanoantennas to control the position of maximum light absorption in the vicinity of an InP energy barrier in InAs nanowires. Comparative photocurrent measurements of the same devices first without and then with the plasmonic nanoantenna demonstrate that the antenna localizes and enhances the optical absorption, in agreement with finite-difference-time-domain (FDTD) simulations. The hot electrons generated in the InAs segment located in the narrow gap of the nanoantenna are subsequently extracted across the InP energy barrier. We study the dependence of the photocurrent and photovoltage on the photon energy and the irradiance of the incident light. When electrons are photoexcited to an energy above the barrier, we find strong evidence that the photocurrent primarily arises from the extraction of hot electrons that have not encountered a significant energy loss due to inelastic scattering. In contrast, when electrons are photoexcited to an energy below the barrier, the photocurrent shows a significantly different dependence on the irradiance of the incident light and can be attributed to photo-thermionic emission.

InAs-InP-InAs nanowire heterostructures were grown by chemical beam epitaxy on (111)B InAs substrates using Au aerosols as seed particles.[30] The nanowires have wurtzite (WZ) crystal structures[30], 61 ± 7 nm diameters, and 67 ± 5 nm InP segment lengths. The nanowire-metal plasmonic nanoantenna devices (Fig. 1(a, b)) were fabricated as follows. First, the nanowires were deposited onto a n-doped Si substrate covered by 200 nm SiO_2. Suitable nanowires were identified by scanning electron microscopy and selected for device fabrication. To add source/drain contacts to the selected nanowires, the samples were spin-coated with resist (poly(methyl methacrylate), PMMA) and electron beam lithography (EBL) was used to create openings for the contacts. The InAs nanowire contact area was etched in a mixture of $(NH_4)_2S_x$ and H_2O 1:20 for 1 min at 40 °C before a film of 25 nm Ni and 75 nm Au was evaporated onto the sample, which was then lifted off in acetone. In a separate step plasmonic antennas were added by repeating the EBL and evaporation of a film of 15 nm Ni and 65 nm Au. Measurements were conducted on the same devices before and after the plasmonic antennas were added. We perform dc photocurrent-voltage measurements based on the circuitry shown in Fig. 1(c) using laser pulses with photon energy $h\nu$ ranging from 0.85 to 1.35 eV and an approximately 30 meV FWHM spectral bandwidth that are generated by a supercontinuum laser with 82 MHz repetition and spectrally selected by a monochromator. The final laser pulse duration is estimated to be ~ 10 ps by considering the bandwidth and spectral broadening in optical fibers that are used in the experiment. Fig. 1(d) shows the approximate band alignment between InAs and InP reported by DFT calculation.[31,32] The FDTD simulations are performed with commercial software Lumerical 3D Electromagnetic Simulator.

In this letter we report data from nine devices, denoted Device I – IX. The scanning electron micrographs and photocurrent measurements of device II and IV are included in the Supplementary Information.

Figure 1 Hot-carrier device and measurement (a, b) Scanning electron micrographs of InAs-InP-InAs heterostructure nanowires with source-drain contacts and (a) a dipole nanoantenna (Device I) and (b) a bow-tie nanoantenna (Device II). The InP segments, serving as energy barriers for energy-selective hot-carrier extraction, are false colored in blue. The purpose of the nanoantenna is to concentrate light absorption into a nanowire volume in the vicinity of one side of the energy barrier[33,34]. (c) Schematic illustration of the hot-carrier device. (d) Schematics of the band alignment of WZ InAs and InP based on band structure parameters from ref.[31,32]. The arrows indicate the electron transition upon interband absorption of photons. Specifically, the red arrow indicates that a minimum photon energy $h\nu$ = 0.95 eV is needed to excite electrons with energy larger than the conduction band barrier (see main text for details).

Figure 2 Photocurrent measurements and FDTD simulations for Device I *without* (top row) and *with* (bottom row) the dipole plasmonic nanoantenna, showing that the plasmonic nanoantenna localizes and enhances optical absorption under TE light. (a, e) Experimentally measured I_{SC} as a function of photon energy $h\nu$ for TM ($\vec{E}$//NW) and TE ($\vec{E}\perp$NW) polarized light. I_{SC} is measured by setting the bias voltage V = 0. The same device was characterized (a) before and (e) after adding the plasmonic antenna in a separate fabrication step. Inset: polarization dependent I_{SC} measured at $h\nu$= (a) 1.25 and (e) 1.20 eV. The error bars represent uncertainties in I_{SC}/ irradiance due to time-dependent fluctuations of the measured I_{SC} caused by fluctuations of charges in the device and light irradiance, and measurement noise. (b, f) FDTD simulation of the absorption efficiency in the nanowire segments between the metal contacts as a function of $h\nu$ for TM and TE polarized light. The dielectric functions of InAs, InP, and Au are obtained from ref. [35–37]. The absorption efficiency is defined as the absorbed power (W) divided by the product of the irradiance of the incident light (Wm^{-2}) and the cross-section of the nanowire segment (m^2). Inset: schematic illustration of the photocurrent-voltage measurement circuitry. (c, d and g, h) FDTD simulation of the $|\vec{E}|^2$ profile at $h\nu$= 1.25 eV for TM and TE polarized light. The device structures are outlined by black lines.

We first performed reference photocurrent measurement on nanowire devices *before* adding the metal nanoantenna (Fig. 2a). In this case, the measured short-circuit current I_{SC} under linearly polarized transverse-magnetic (TM) light was larger than under transverse-electric (TE) light for the entire spectral range ($h\nu$= 0.85 - 1.35 eV). The observed anisotropic photocurrent generation is consistent with the anisotropic light absorption shown by the FDTD simulation in Fig. 2 (b-d). The enhancement of the TM-polarized light field in the nanowire and near the nanowire-metal contacts can be attributed to leaky-mode resonance[38,39] and plasmonic effects[27], respectively.

Adding the gold dipole (Device I) or bow-tie (Device II) nanoantennas greatly increased I_{SC} under TE-polarized light, making it much larger than under TM-polarized for $h\nu$ < 1.25 eV (Fig. 2e). Furthermore, as shown in Fig. 2(e) inset, the polarization dependence was completely changed upon adding the antenna. This experimental result is consistent with the FDTD simulation in that the light absorption is strongly enhanced under TE-polarized light (Fig. 2(f-h)), in particular locally in the gap of the nanoantennas. The FDTD simulation of Device I and II shows that the absorption efficiency increases by a factor of ~30 within the nanowire segment between the metal contacts for the studied spectrum and by a factor of more than 100 locally within the gap of the nanoantennas. In comparison, the $|I_{SC}|$ enhancement varies significantly with $h\nu$ (from ~5 to ~100 in Device I). The main reason is that the in devices without nanoantennas, the light absorption is not localized near the InP barrier, such that photocurrent can be generated through alternative mechanisms instead of internal photoemission across the InP barrier. Therefore, I_{SC} in devices without nanoantennas exhibits a different dependency on photon energy and significant variations between devices.In addition, the polarity of I_{SC} corresponds to a net flow of electrons from the nanoantenna towards the barrier, consistent with the physical picture that photoexcited hot electrons

(instead of hot holes) are dominantly extracted across the barrier as a result of the smaller electron effective mass in InAs, which will be discussed in detail later on. We observe similar I_{SC} increase after adding nanoantennas and correlations between the polarity of I_{SC} with the antenna-barrier direction in a total of eight devices (see supplementary information (SI) for Devices II and IV - IX).

It is worth noting that although the nanoantennas are in physical contact with the nanowires due to EBL misalignment and proximity effect, the native oxides on the nanowires usually create a large contact resistance (> 100 kΩ)[40]. In addition, the nanoantennas are not electrically connected otherwise. Therefore, we expect that hot carriers generated in the Au nanoantennas will unlikely transfer into the nanowires and that the photocurrent is primarily contributed by photo-carriers generated by interband absorption in InAs for $h\nu$ larger than the InAs band gap. This assumption is further confirmed as the experimentally measured I_{SC} and open-circuit spectrum can be well explained by the transport of photoexcited hot carriers in InAs, which are discussed throughout the rest of the letter.

So far, we have shown that by adding nanoantennas to the nanowire devices, the absorption of TE-polarized light is strongly enhanced in the gap of the nanoantenna, which can be controlled to achieve high asymmetry relative to the InP barrier. In the following we will investigate the energy distribution and extraction process of the photoexcited electrons in such nanowire-nanoantenna devices under TE-polarized light based on the I_{SC} and the open-circuit voltage V_{OC} measurements.

We find that I_{SC} per irradiance increases with $h\nu$ (Fig. 3(a)). However, I_{SC} exhibits significantly different dependence on the irradiance for large and small $h\nu$: I_{SC} increases linearly with irradiance for $h\nu > 1$ eV (Fig. 3(b)) and nonlinearly for $h\nu < 1$ eV (Fig.3(c)). In the following, we will interpret this experimental result based on the semiclassical three-step model discussed in the following, where the photocurrent generation process is separated into: (1) hot-carrier excitation, (2) hot-carrier transport to the barrier interface, and (3) hot-carrier emission over the barrier (Fig. 3d).[14,19,41]

Figure 3 I_{SC} dependence on photon energy and irradiance for Device I: (a) I_{SC} measured as a function of $h\nu$ at two irradiances. The experimental data (dots) is fitted with Eq. 3, which is based on the internal photoemission theory (dashed line). (b) I_{SC} increases nonlinearly with irradiance for $h\nu$ = 0.80, 0.85, and 0.90 eV and (c) linearly with irradiance for $h\nu$ = 1.1, 1.2, and 1.3 eV. (d) Schematics of the three-step photoemission model: (1) hot-carrier excitation, (2) hot-carrier transport to the barrier interface, and (3) hot-carrier emission over the barrier. The error bar in (a-c) represents the time-dependent fluctuations of the measured I_{SC}.

(1) Excitation. In the first step, hot carriers are excited in the nanowire. The spatial distribution of hot-carrier generation can be readily obtained from the FDTD simulation. The energy distribution of electrons and holes excited through interband absorption of photons with a given energy $h\nu$ can be inferred from the electronic band structure based on the energy conservation relation $E_e(k) - E_h(k) = h\nu$. In Fig. 4(a, b) the approximate band structure of WZ InAs calculated based on k•p theory[32] and the energy distribution of photoexcited electrons and holes for $h\nu$ = 1.24 eV are shown. Within this approximation, the energy distribution of the photoexcited electrons and holes are separated into three groups as a result of the heavy hole, crystal field split-off hole, and light hole valence bands. Due to the large effective mass and density of states of the heavy-hole band, the majority of the photoexcited electrons initially obtain most of the photon energy in excess of the band gap, while the majority of the photoexcited holes lies near the band edge and below the barrier in the valence band, as show in Fig. 4(b).

Figure 4. (a) Electronic band structure of WZ InAs calculated based on k•p theory with parameters from ref.[32] except that the conduction band energy E_c is reduced by 0.1 eV to obtain WZ InAs band gap E_g = 0.37 eV in the range observed in previous transport[42] and scanning tunneling spectroscopy[43] experiments. The black arrows indicate interband transitions for $h\nu$ = 1.24. (b) Distribution of photoexcited electrons and holes for $h\nu$ = 1.24 eV calculated based on the band structure and energy conservation of the interband absorption process. (c) The calculated energy dependent barrier transmission function for electrons (blue) and holes (red). The electron and hole barrier energies (dotted line) are E_b = 0.56 eV and E_{bv} = 0.38 eV,[31] respectively.

(2) Transport. In the second step, as the hot carriers transport towards the barrier interface, inelastic scattering will gradually lead to thermalization among the carriers and with the lattice. For photoexcited electrons or holes that arrive at the barrier interface without encountering any significant energy loss, their emission over the barrier is usually referred to as *internal photoemission*.[13,19] Thus, if the scattering rate is independent of carrier density, I_{SC} can be expected to increase linearly with the generation rate of hot electrons or holes. In contrast, if the hot carriers near the barrier are thermalized, the photocurrent is generated through emission of electrons occupying high energy states (*photo-thermionic emission*). In this case, I_{SC} is expected to increase exponentially with the effective temperature of the hot electrons ($\sim \exp[(\mu - E_b)/kT_e]$) and to have a nonlinear dependence on the incident light intensity.

(3) Emission. Finally, in the third step, the emission of hot electrons and holes over the barrier is characterized by the barrier's transmission probability $T(E_{e,h})$. Given the InP barrier thickness of > 60 nm, we can effectively rule out tunneling. Therefore, for internal photoemission, we can estimate that a minimum $h\nu$ = 0.95, 2.30, 1.60 and 0.82 eV is needed for the emission of electrons, heavy holes, crystal field split-off holes, and light holes, respectively, based on the barrier heights (E_b = 0.56 eV for electrons and E_{bh} = 0.38 eV for holes as obtained from Ref. [31]) and the calculated electronic band structure (Fig. 4(a)). While internal photoemission of light holes is possible for the entire spectral range in the experiment (0.85 - 1.35 eV), the observed polarity of I_{SC} suggests that the light-hole contribution is small compared to that of electrons, consistent with the light holes' small density of states. In the theoretical discussions below we will therefore focus on electron emission and disregard hole emission. We calculate $T(E_{e,h})$ by summing up the transmission probability of each 1D subband, which is obtained by solving the Schrödinger's equation[22] (see SI for details). As we assume that the lateral momentum needs to be conserved, $T(E_{e,h})$ shows a slow increase instead of a step function at $E_e = E_b$ and $E_h = E_{bh}$, as shown in Fig. 4(c).

The estimated threshold for the internal photoemission of electrons at $h\nu$ = 0.95 eV is consistent with the transition between nonlinear and linear dependence of I_{SC} on the irradiance observed in the experiment (Fig. 3 (b, c)). We therefore infer that I_{SC} arises dominantly from internal photoemission for $h\nu \geq 0.95$ eV and we can model I_{SC} based on the three-step model as

$$I_{SC}(h\nu) = \frac{e}{2}\iint Q(x,E_e)e^{\frac{-x}{\Lambda}}T(E_e)dxdE, \qquad \text{Eq. 3}$$

where $Q(x, E_e)$ represents the generation rate of hot electrons with energy E_e per length at distance x from the barrier. The factor of 1/2

describes that only half of the photoexcited electrons are expected to transport toward the barrier, and $e^{\frac{-x}{\Lambda}}$ characterizes the decay of hot electrons from their initial high energy states E_e with inelastic scattering length Λ.

We find a good agreement between Eq. 3 and the measured I_{SC} by using, as the only fitting parameter, $\Lambda = 14.0 \pm 0.5$ nm for Device I (Fig. 3(a)). By fitting I_{SC} of Device II and IV, we found $\Lambda = 30.0 \pm 2.3$ and 34.8 ± 3.0 nm (see SI). The calculation reveals that the strong photon energy dependence of I_{SC} can be largely attributed to the dependence of the transmission probability on E_e. For $E_e \approx E_b$ (0.56 eV), the electron velocity is around 2×10^6 m/s and Λ corresponds to an inelastic scattering time on the order of $\approx$ 10 fs, which is on the same order of magnitude as the electron-electron scattering time measured in bulk III-V semiconductors using high excitation photon energy.[1,44] Based on the FDTD simulation of the optical absorption, the internal quantum efficiency is estimated to be up to 0.5 – 1.2 % for Device I, II, and IV at larger $h\nu$.

Important for hot-carrier photovoltaic applications, the high kinetic energy of hot electrons is expected to result in a large open-circuit voltage V_{OC}. In the case of internal photoemission, the maximally achievable open-circuit voltage $V_{OC,max}$ is the electrostatic potential required to raise the effective barrier height to reflect electrons with the highest energy $E_{e,max}$, as indicated in Fig. 5(a). In this simple picture, $V_{OC,max}$ can be expressed as

$$eV_{OC,max} = E_{e,max} - E_b, \qquad \text{Eq. 4}$$

independent of the irradiance of incident light, as observed previously in metal-insulator-metal devices.[14,45] However, a V_{OC} close to $V_{OC,max}$ can only be obtained when the dark current and the reverse current due to hole emission, and light absorption on the opposite side of the barrier, are negligible.

We extracted V_{OC} for three devices from photocurrent-voltage measurements (Fig.5 (b)). For $h\nu$ = 1.0 – 1.2 eV, V_{OC} increases roughly linear with $h\nu$, consistent with $V_{OC,max}$ in Eq. 4 (Fig. 5(c)). Moreover, the measured V_{OC} is insensitive to the optical irradiance, which is varied by more than an order of magnitude (Fig. 5(d)).

Fig.5 Open circuit voltage: (a) Schematics of the open-circuit condition described by Eq. 4. (b) Photocurrent-voltage measurement for $h\nu$ = 1.0, 1.1, 1.2, and 1.3 eV. (c) Experimentally measured V_{OC} (Device I, II, III) and $(E_e\text{-}E_b)/e$ as a function of $h\nu$. (d) V_{OC} (Device II) as a function of incident light irradiance normalized by the maximum irradiance for each $h\nu$. The error bars in (c, d) represent the uncertainties in the extracted V_{OC} due to time-dependent current fluctuations.

However, for $h\nu > 1.1$ eV, we observe a large variation of V_{OC} between devices where some of them exhibit a clear deviation from Eq. 4 (Fig. 5 (c)). We attribute the breakdown of the approximation in Eq. 4 to the increased importance of optical absorption outside the nanoantenna region at larger $h\nu$. First, it can be observed in Fig. 2 (a) and Fig. S1 (e,f) in the SI that, in the absence of the nanoantenna, I_{SC} has an onset at $h\nu$ = 1.1 – 1.2 eV under TE-polarized light. In addition, I_{SC} of Device I shows an opposite polarity after the nanoantenna was added (Fig. 2 (d)), which indicates that the optical absorption outside the nanoantenna region creates a current in the opposite direction from the absorption within the gap of the nanoantenna, such that a V_{OC} lower than $V_{OC,max}$ can be expected. In comparison, I_{SC} of Device II has the same polarity with and without nanoantenna, which is consistent with its larger V_{OC} that is in good agreement with Eq. 4 up to $h\nu \sim 1.2$ eV. Based on the device structures and the simulated absorption profiles of Device I and II (Fig. S3), their opposite I_{SC} polarity before the nanoantennas were added cannot be explained by only considering internal photoemission across the InP energy barrier, especially as the inelastic scattering lengths extracted here are only around tens of nanometers. Instead, as discussed earlier, the opposite polarity indicates that light absorption away from the InP barrier can result in photocurrent generation through alternative mechanisms. For example, photo-excited electrons and holes can be separated by electric fields resulting from unintentional inhomogeneous doping[46] and Schottky contacts between the nanowire and the source/ drain contact[47].At even higher $h\nu$, we expect reverse photocurrent due to hole excitations and photoexcitation in the InP barrier to also reduce V_{OC} from the maximum value given in Eq. 4.

So far we have shown that for $h\nu > 1$ eV, hot electrons are excited to energies above the InP barrier. The dependencies of I_{SC} and V_{OC} on $h\nu$ and irradiance reveal that they are dominantly generated through extracting hot electrons before these encounter any significant energy loss through inelastic scattering. The measured I_{SC} and V_{OC} are in good agreements with theoretical predictions based on the internal photoemission effect.

However, the internal photoemission effect doesn't account for I_{SC} generated with incident light with $h\nu < 1$ eV. Instead, the observed nonlinear dependence of the I_{SC} on the irradiance in this photon energy range (Fig. 3b) is consistent with the photo-thermionic effect.[18] For $h\nu < 1$ eV, photoexcited electrons initially do not have enough energy to surmount the energy barrier, yet some high-energy states are occupied after the energy is redistributed through electron-electron scattering. When the electrons are equilibrated, the energy distribution will follow Fermi-Dirac statistics with a well-defined electron temperature T_e (which may be much higher than the lattice temperature) and quasi-Fermi level $E_{F,e}$[48]. Photocurrent generated through thermionic emission can be expected to be proportional to $T_e^2\exp[(E_{F,e}\text{-}E_b)/kT_e]$[49], which can have a highly nonlinear dependence on the irradiance.

For the light irradiance used in this study, we expect the mean temperature increase in the nanowire due to light absorption to be very small (< 1 K) taking into account thermal conduction to the metal contacts and the substrate.[50] However, due to the large excess photon energy and the laser pulse width of ~10 ps, for light irradiance of 10^3 to 10^5 Wm^{-2} used in this study (this roughly corresponds to a photoexcited charge carrier density of 10^{16} – 10^{18} cm^{-3}, considering an absorption efficiency between 5 – 10 in the gap of the nanoantennas), we expect the electron temperature to rise by up to a few hundred Kelvin within a few ps after the absorption of the laser pulse[1,51,52]. The actual temperature evolution as a function of time and space will require elaborate experiment and simulation, and is outside the scope of this study.

Based on the photocurrent measurements (Fig. 3(a-c)), we observe that photo-thermionic emission has a much lower internal quantum efficiency compared to internal photoemission. At $h\nu$ = 0.95 eV, where the internal photoemission is expected to be vanishingly small, the internal quantum efficiency is estimated to be less than 0.05 % for 6.7×10^4 Wm^{-2} irradiance. Based on the thermionic emission equation, we can expect to increase the efficiency by implementing a lower energy barrier. In addition one can implement strategies to increase T_e and $E_{F,e}$, such as reducing the energy loss pathways and increasing the light intensity. However, it's worth mentioning that the irradiance used in this study is already larger than the typical solar irradiance on Earth's surface[53].

We want to point out that although internal photoemission based on multiphoton absorption can also lead to a nonlinear photocurrent dependence on the light irradiance,[54] but can be readily distinguished from the photo-thermionic effect based on V_{OC} measurements because the energy distribution of the photoexcited carriers would be very different.[55] For instance, based on Eq. 4 we would expect a large V_{OC} as a result of the high kinetic energy of electrons generated through two-photon absorptions ($E_e \sim (2h\nu - E_g)/(1+m_e/m_h)$ based on the effective mass approximation). However, we observe minuscule V_{OC} for all three devices in the experiment (Fig. 5(c)).

In summary, we realized an optical hot-carrier device based on an InAs-InP-InAs heterostructure nanowire equipped with a metal plasmonic nanoantenna. The nanoantenna enhances light absorption over a broad spectrum and allows to define the location of hot carrier generation in a subwavelength region. This is not only important for achieving highly asymmetric light absorption as a pre-requisite to increasing internal quantum efficiency, but also enables us to understand the extraction process of hot electrons based on the photocurrent-voltage measurements. We observed that when the energy of photoexcited electrons is larger than the energy barrier, they dominantly contribute to the photocurrent through internal photoemission. On the contrary, photocurrent created by photoexcited electrons with less energy than the barrier shows nonlinear power dependence characteristic of photo-thermionic emission.

The findings in this study provide helpful guidelines to increase I_{SC} and V_{OC} in hot-carrier devices based on nanowire heterostructures. The enhancement of I_{SC} observed in the present study is most likely bounded by experimental limitations. If nanoantennas can be made with sharper features, smoother surfaces, and smaller gaps, light-field enhancement in the gap of the nanoantenna is expected to increase by several orders of magnitude.[56–58] Moreover, the internal quantum efficiency can likely be improved by reducing losses in each step of the three-step internal photoemission model[14,19,41], which, as we have shown, provides a prediction consistent with the measured I_{SC}. First, half of the photoexcited electrons initially transporting away from the barrier may be collected by implementing an additional barrier. Second, the electron relaxation length extracted here (tens of nm) provides an estimate of the requirement to concentrate the light field near the barrier in order to reduce loss due to inelastic scattering in such nanowire systems. Such strong concentration can potentially be realized by taking advantage of nanophotonic effects. Finally, we can remedy the loss caused by the reflection of electrons with energy near or lower the energy barrier by reducing InP segment length, and engineering the band alignment[59] and effective mass of the heterostructure to optimize the transmission probability for a given input light spectrum. Therefore, in an ideal device, the I_{SC} enhancement may surpass what was observed in this study by several orders of magnitude. As for V_{OC}, we demonstrated values that are close to the theoretical upper limit for a range of $h\nu$. We expect that by carefully engineering light absorption outside the nanoantenna region, V_{OC} equal to the upper limit can be realized for the full range of $h\nu$ when photocurrent is dominantly generated through internal photoemission and as long as light absorption in the barrier is negligible.

Supplementary information

Additional materials including photocurrent measurements and analysis of Device II and IV, and details of the calculation of electron transmission probability across an energy barrier in a nanowire, are available in the supplementary information.

Acknowledgement

The authors thank Lukas Wittenbecher and Anders Mikkelsen for their help with the optical modelling and acknowledge financial support from the European Research Council under the European Union's Seventh Framework Programme (FP/2007-2013)/ERC Grant Agreement No. 336126; the People Programme of the European Union (Marie Curie Actions, FP7-People-2013-ITN) Grant No. n°608153; PhD4Energy; the Swedish Research Council (VR); and the Knut and Alice Wallenberg Foundation (KAW), project 2016.0089.

References:

1. *Hot Carriers in Semiconductor Nanostructures*; Shah, J., Ed.; Academic Press: Boston, MA, 1992.

2. Sze, S. M.; Ng, K. K. *Physics of Semiconductor Devices*; John Wiley & Sons, Inc.: Hoboken, NJ, 2006.

3. Shockley, W.; Queisser, H. J. Detailed Balance Limit of Efficiency of P-n Junction Solar Cells. *J. Appl. Phys.* **1961**, *32* (3), 510–519.

4. Hirst, L. C.; Ekins-Daukes, N. J. Fundamental Losses in Solar Cells. *Prog. Photovoltaics Res. Appl.* **2011**, *19* (3), 286–293.

5. J. E., B.; Y. G., W. High-Speed Photodetectors. In *Handbook of Optics: Fundamentals, techniques, and design, Volume 1*; Bass, M., Ed.; McGraw-Hill: New York, NY, 1994.

6. *Handbook of Optoelectronics, 2E, Vol1*; Dakin, J., Brown, R., Eds.; Series in Optics and Optoelectronics; CRC Press: Boca Raton, FL, 2017.

7. Ross, R. T.; Nozik, A. J. Efficiency of Hot-Carrier Solar Energy Converters. *J. Appl. Phys.* **1982**, *53* (5), 3813–3818.

8. Würfel, P. Solar Energy Conversion with Hot Electrons from Impact Ionisation. *Sol. Energy Mater. Sol. Cells* **1997**, *46* (1), 43–52.

9. Limpert, S.; Bremner, S.; Linke, H. Reversible Electron–Hole Separation in a Hot Carrier Solar Cell. *New J. Phys.* **2015**, *17* (9), 095004.

10. Dimmock, J. A. R.; Day, S.; Kauer, M.; Smith, K.; Heffernan, J. Demonstration of a Hot-Carrier Photovoltaic Cell. *Prog. Photovoltaics Res. Appl.* **2014**, *22* (2), 151–160.

11. Dimmock, J. A. R.; Kauer, M.; Stavrinou, P. N.; Ekins-Daukes, N. J. A Metallic Hot Carrier Photovoltaic Cell; Freundlich, A., Guillemoles, J.-F., Sugiyama, M., Eds.; 2015; p 935810.

12. Josefsson, M.; Svilans, A.; Burke, A. M.; Hoffmann, E. A.; Fahlvik, S.; Thelander, C.; Leijnse, M.; Linke, H. A Quantum-Dot Heat Engine Operating Close to the Thermodynamic Efficiency Limits. *Nat. Nanotechnol.* **2018**, *13* (10), 920–924.

13. Knight, M. W.; Sobhani, H.; Nordlander, P.; Halas, N. J. Photodetection with Active Optical Antennas. *Science (80-.).* **2011**, *332* (6030), 702–704.

14. Wang, F.; Melosh, N. A. Plasmonic Energy Collection

through Hot Carrier Extraction. *Nano Lett.* **2011**, *11* (12), 5426–5430.

15. Chalabi, H.; Schoen, D.; Brongersma, M. L. Hot-Electron Photodetection with a Plasmonic Nanostripe Antenna. *Nano Lett.* **2014**, *14* (3), 1374–1380.

16. Nakpathomkun, N.; Xu, H. Q.; Linke, H. Thermoelectric Efficiency at Maximum Power in Low-Dimensional Systems. *Phys. Rev. B* **2010**, *82* (23), 235428.

17. Schwede, J. W.; Sarmiento, T.; Narasimhan, V. K.; Rosenthal, S. J.; Riley, D. C.; Schmitt, F.; Bargatin, I.; Sahasrabuddhe, K.; Howe, R. T.; Harris, J. S.; et al. Photon-Enhanced Thermionic Emission from Heterostructures with Low Interface Recombination. *Nat. Commun.* **2013**, *4* (1), 1576.

18. Massicotte, M.; Schmidt, P.; Vialla, F.; Watanabe, K.; Taniguchi, T.; Tielrooij, K. J.; Koppens, F. H. L. Photo-Thermionic Effect in Vertical Graphene Heterostructures. *Nat. Commun.* **2016**, *7*, 12174.

19. Leenheer, A. J.; Narang, P.; Lewis, N. S.; Atwater, H. A. Solar Energy Conversion via Hot Electron Internal Photoemission in Metallic Nanostructures: Efficiency Estimates. *J. Appl. Phys.* **2014**, *115* (13), 134301.

20. Björk, M. T.; Ohlsson, B. J.; Sass, T.; Persson, A. I.; Thelander, C.; Magnusson, M. H.; Deppert, K.; Wallenberg, L. R.; Samuelson, L. One-Dimensional Steeplechase for Electrons Realized. *Nano Lett.* **2002**, *2* (2), 87–89.

21. Kim, R.; Jeong, C.; Lundstrom, M. S. On Momentum Conservation and Thermionic Emission Cooling. *J. Appl. Phys.* **2010**, *107* (5), 054502.

22. Levy-Leblond, J.-M. Elementary Quantum Models with Position-Dependent Mass. *Eur. J. Phys.* **1992**, *13* (5), 215–218.

23. Tedeschi, D.; De Luca, M.; Fonseka, H. A.; Gao, Q.; Mura, F.; Tan, H. H.; Rubini, S.; Martelli, F.; Jagadish, C.; Capizzi, M.; et al. Long-Lived Hot Carriers in III–V Nanowires. *Nano Lett.* **2016**, *16* (5), 3085–3093.

24. Shojaei, I. A.; Linser, S.; Jnawali, G.; Wickramasuriya, N.; Jackson, H. E.; Smith, L. M.; Kargar, F.; Balandin, A. A.; Yuan, X.; Caroff, P.; et al. Strong Hot Carrier Effects in Single Nanowire Heterostructures. *Nano Lett.* **2019**, *19* (8), 5062–5069.

25. Sakaki, H. Scattering Suppression and High-Mobility Effect of Size-Quantized Electrons in Ultrafine Semiconductor Wire Structures. *Jpn. J. Appl. Phys.* **1980**, *19* (12), L735–L738.

26. Cao, L.; White, J. S.; Park, J.-S.; Schuller, J. A.; Clemens, B. M.; Brongersma, M. L. Engineering Light Absorption in Semiconductor Nanowire Devices. *Nat. Mater.* **2009**, *8* (8), 643–647.

27. Maier, S. A. *Plasmonics: Fundamentals and Applications*; Springer US: New York, NY, 2007.

28. Limpert, S.; Burke, A.; Chen, I.-J.; Anttu, N.; Lehmann, S.; Fahlvik, S.; Bremner, S.; Conibeer, G.; Thelander, C.; Pistol, M.-E.; et al. Single-Nanowire, Low-Bandgap Hot Carrier Solar Cells with Tunable Open-Circuit Voltage. *Nanotechnology* **2017**, *28* (43), 434001.

29. Limpert, S.; Burke, A.; Chen, I. J.; Anttu, N.; Lehmann, S.; Fahlvik, S.; Bremner, S.; Conibeer, G.; Thelander, C.; Pistol, M. E.; et al. Bipolar Photothermoelectric Effect Across Energy Filters in Single Nanowires. *Nano Lett.* **2017**, *17* (7), 4055–4060.

30. Fahlvik Svensson, S.; Jeppesen, S.; Thelander, C.; Samuelson, L.; Linke, H.; Dick, K. A. Control and Understanding of Kink Formation in InAs–InP Heterostructure Nanowires. *Nanotechnology* **2013**, *24* (34), 345601.

31. Hajlaoui, C.; Pedesseau, L.; Raouafi, F.; Ben Cheikh Larbi, F.; Even, J.; Jancu, J.-M. First-Principles Calculations of Band Offsets and Polarization Effects at InAs/InP Interfaces. *J. Phys. D. Appl. Phys.* **2015**, *48* (35), 355105.

32. Faria Junior, P. E.; Campos, T.; Bastos, C. M. O.; Gmitra, M.; Fabian, J.; Sipahi, G. M. Realistic Multiband K·p Approach from Ab Initio and Spin-Orbit Coupling Effects of InAs and InP in Wurtzite Phase. *Phys. Rev. B* **2016**, *93* (23), 235204.

33. Cubukcu, E.; Nanfang Yu; Smythe, E. J.; Diehl, L.; Crozier, K. B.; Capasso, F. Plasmonic Laser Antennas and Related Devices. *IEEE J. Sel. Top. Quantum Electron.* **2008**, *14* (6), 1448–1461.

34. Biagioni, P.; Huang, J.-S.; Hecht, B. Nanoantennas for Visible and Infrared Radiation. *Reports Prog. Phys.* **2012**, *75* (2), 024402.

35. Aspnes, D. E.; Studna, A. A. Dielectric Functions and Optical Parameters of Si, Ge, GaP, GaAs, GaSb, InP, InAs, and InSb from 1.5 to 6.0 EV. *Phys. Rev. B* **1983**, *27* (2), 985–1009.

36. *Handbook of Optical Constants of Solids*; Palik, E. D., Ed.; Elsevier: New York, NY, 1985.

37. Olmon, R. L.; Slovick, B.; Johnson, T. W.; Shelton, D.; Oh, S.-H.; Boreman, G. D.; Raschke, M. B. Optical Dielectric Function of Gold. *Phys. Rev. B* **2012**, *86* (23), 235147.

38. Cao, L.; White, J. S.; Park, J.-S.; Schuller, J. A.; Clemens, B. M.; Brongersma, M. L. Engineering Light Absorption in Semiconductor Nanowire Devices. *Nat. Mater.* **2009**, *8* (8), 643–647.

39. Hosseinnia, A.; Anttu, N. Absorption through a Coupled Optical Resonance in a Horizontal InP Nanowire Array. *Photonics Res.* **2015**, *3* (4), 125–128.

40. Suyatin, D. B.; Thelander, C.; Björk, M. T.; Maximov, I.; Samuelson, L. Sulfur Passivation for Ohmic Contact Formation to InAs Nanowires. *Nanotechnology* **2007**.

41. Afanas'ev, V. V. *Internal Photoemission Spectroscopy Fundamentals and Recent Advances*; Elsevier: Amsterdam, 2014.

42. Chen, I.-J.; Lehmann, S.; Nilsson, M.; Kivisaari, P.; Linke, H.; Dick, K. A.; Thelander, C. Conduction Band Offset and Polarization Effects in InAs Nanowire Polytype Junctions. *Nano Lett.* **2017**, *17* (2), 902–908.

43. Hjort, M.; Lehmann, S.; Knutsson, J.; Zakharov, A. A.; Du, Y. A.; Sakong, S.; Timm, R.; Nylund, G.; Lundgren, E.; Kratzer, P.; et al. Electronic and Structural Differences between Wurtzite and Zinc Blende Inas Nanowire Surfaces: Experiment and Theory. *ACS Nano* **2014**, *8* (12), 12346–12355.

44. Lin, W. Z.; Fujimoto, L. G.; Ippen, E. P.; Logan, R. A. Femtosecond Carrier Dynamics in GaAs. *Appl. Phys. Lett.* **1987**, *50* (3), 124–126.

45. Wang, F.; Melosh, N. A. Power-Independent Wavelength Determination by Hot Carrier Collection in Metal-Insulator-Metal Devices. *Nat. Commun.* **2013**, *4* (1), 1711.

46. Ning, Z.; Zhitomirsky, D.; Adinolfi, V.; Sutherland, B.; Xu, J.; Voznyy, O.; Maraghechi, P.; Lan, X.; Hoogland, S.; Ren, Y.; et al. Graded Doping for Enhanced Colloidal Quantum Dot Photovoltaics. *Adv. Mater.* **2013**, *25* (12), 1719–1723.

47. Gu, Y.; Kwak, E.-S.; Lensch, J. L.; Allen, J. E.; Odom, T. W.; Lauhon, L. J. Near-Field Scanning Photocurrent Microscopy of a Nanowire Photodetector. *Appl. Phys. Lett.* **2005**, *87* (4), 043111.

48. Shah, J. *Ultrafast Spectroscopy of Semiconductors and Semiconductor Nanostructures*; Springer Series in Solid-State Sciences; Springer Berlin Heidelberg: Berlin, Heidelberg, 1999; Vol. 115.

49. Yang, K.; East, J. R.; Haddad, G. I. Numerical Modeling of Abrupt Heterojunctions Using a Thermionic-Field Emission Boundary Condition. *Solid State Electron.* **1993**, *36* (3), 321–330.

50. Könemann, F.; Chen, I.-J.; Lehmann, S.; Thelander, C.; Gotsmann, B. Imaging the Thermalization of Hot Carriers After Thermionic Emission Over a Polytype Barrier. **2019**, arXiv:1911.11415 [cond-mat.mes-hall]. http://arxiv.org/abs/1911.11415 (November 26, 2019)

51. Wang, Y.; Jackson, H. E.; Smith, L. M.; Burgess, T.; Paiman, S.; Gao, Q.; Tan, H. H.; Jagadish, C. Carrier Thermalization Dynamics in Single Zincblende and Wurtzite InP Nanowires. *Nano Lett.* **2014**, *14* (12), 7153–7160.

52. Yong, C. K.; Wong-Leung, J.; Joyce, H. J.; Lloyd-Hughes, J.; Gao, Q.; Tan, H. H.; Jagadish, C.; Johnston, M. B.; Herz, L. M. Direct Observation of Charge-Carrier Heating at WZ–ZB InP Nanowire Heterojunctions. *Nano Lett.* **2013**, *13* (9), 4280–4287.

53. Rühle, S. Tabulated Values of the Shockley–Queisser Limit for Single Junction Solar Cells. *Sol. Energy* **2016**, *130*, 139–147.

54. Sivis, M.; Pazos-Perez, N.; Yu, R.; Alvarez-Puebla, R.; García de Abajo, F. J.; Ropers, C. Continuous-Wave Multiphoton Photoemission from Plasmonic Nanostars. *Commun. Phys.* **2018**, *1* (1), 13.

55. Logothetis, E. M.; Hartman, P. L. Laser-Induced Electron Emission from Solids: Many-Photon Photoelectric Effects and Thermionic Emission. *Phys. Rev.* **1969**, *187*, 460.

56. Ciraci, C.; Hill, R. T.; Mock, J. J.; Urzhumov, Y.; Fernandez-Dominguez, A. I.; Maier, S. A.; Pendry, J. B.; Chilkoti, A.; Smith, D. R. Probing the Ultimate Limits of Plasmonic Enhancement. *Science (80-.).* **2012**, *337* (6098), 1072–1074.

57. Khurgin, J.; Tsai, W.-Y.; Tsai, D. P.; Sun, G. Landau Damping and Limit to Field Confinement and Enhancement in Plasmonic Dimers. *ACS Photonics* **2017**, *4* (11), 2871–2880.

58. Alcaraz Iranzo, D.; Nanot, S.; Dias, E. J. C.; Epstein, I.; Peng, C.; Efetov, D. K.; Lundeberg, M. B.; Parret, R.; Osmond, J.; Hong, J.-Y.; et al. Probing the Ultimate Plasmon Confinement Limits with a van Der Waals Heterostructure. *Science (80-.).* **2018**, *360* (6386), 291–295.

59. Zhao, Z. C.; McKenzie, D. R. Antireflection Coating of Barriers to Enhance Electron Tunnelling: Exploring the Matter Wave Analogy of Superluminal Optical Phase Velocity. *Sci. Rep.* **2017**, *7* (1), 12772.

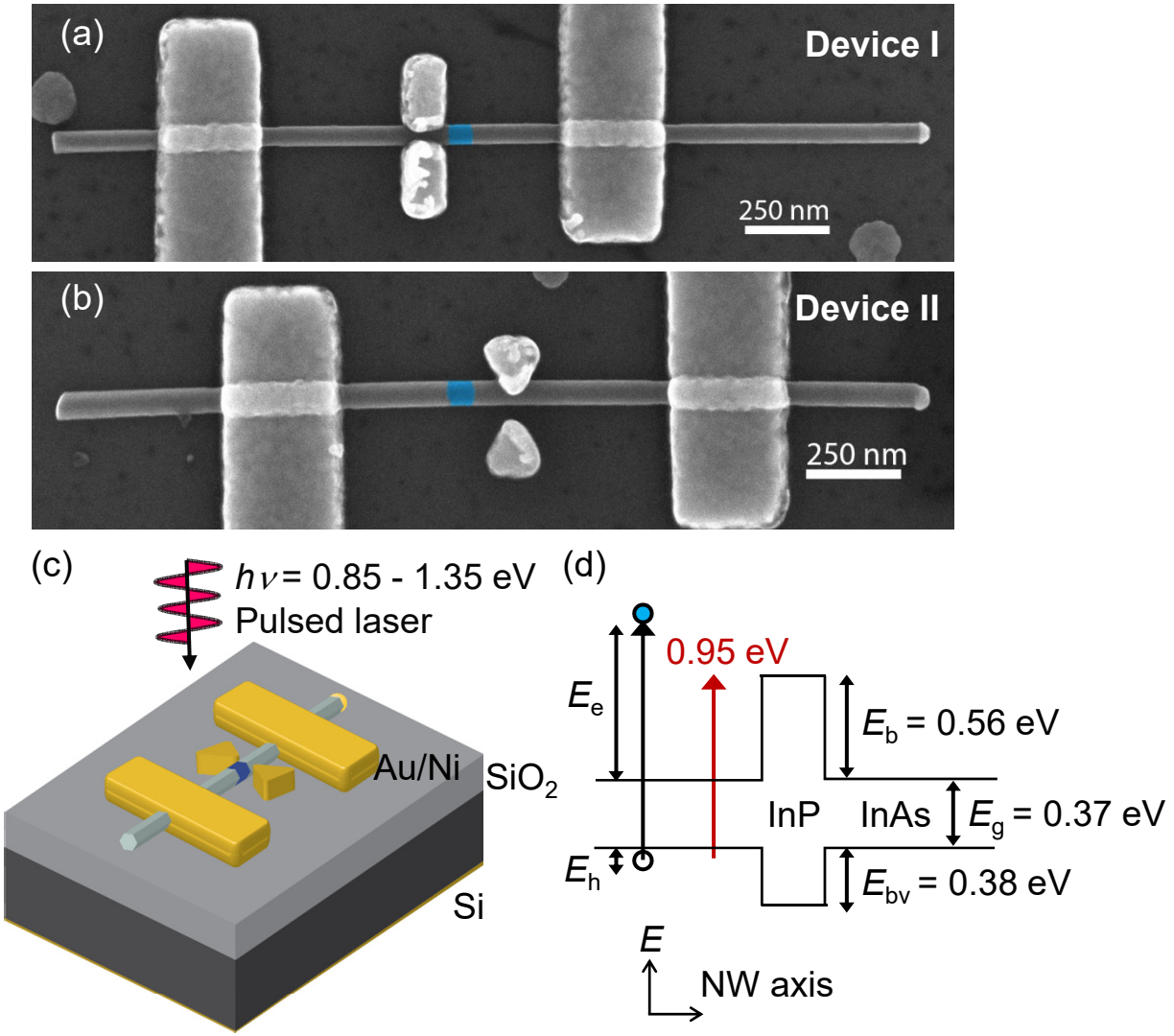
(a)
Device I
250 nm
(b)
Device II
250 nm
(c)
hν = 0.85 - 1.35 eV
Pulsed laser
Au/Ni
SiO2
Si
(d)
0.95 eV
Ee
Eb = 0.56 eV
InP
InAs
Eg = 0.37 eV
Eh
Ebv = 0.38 eV
E
NW axis

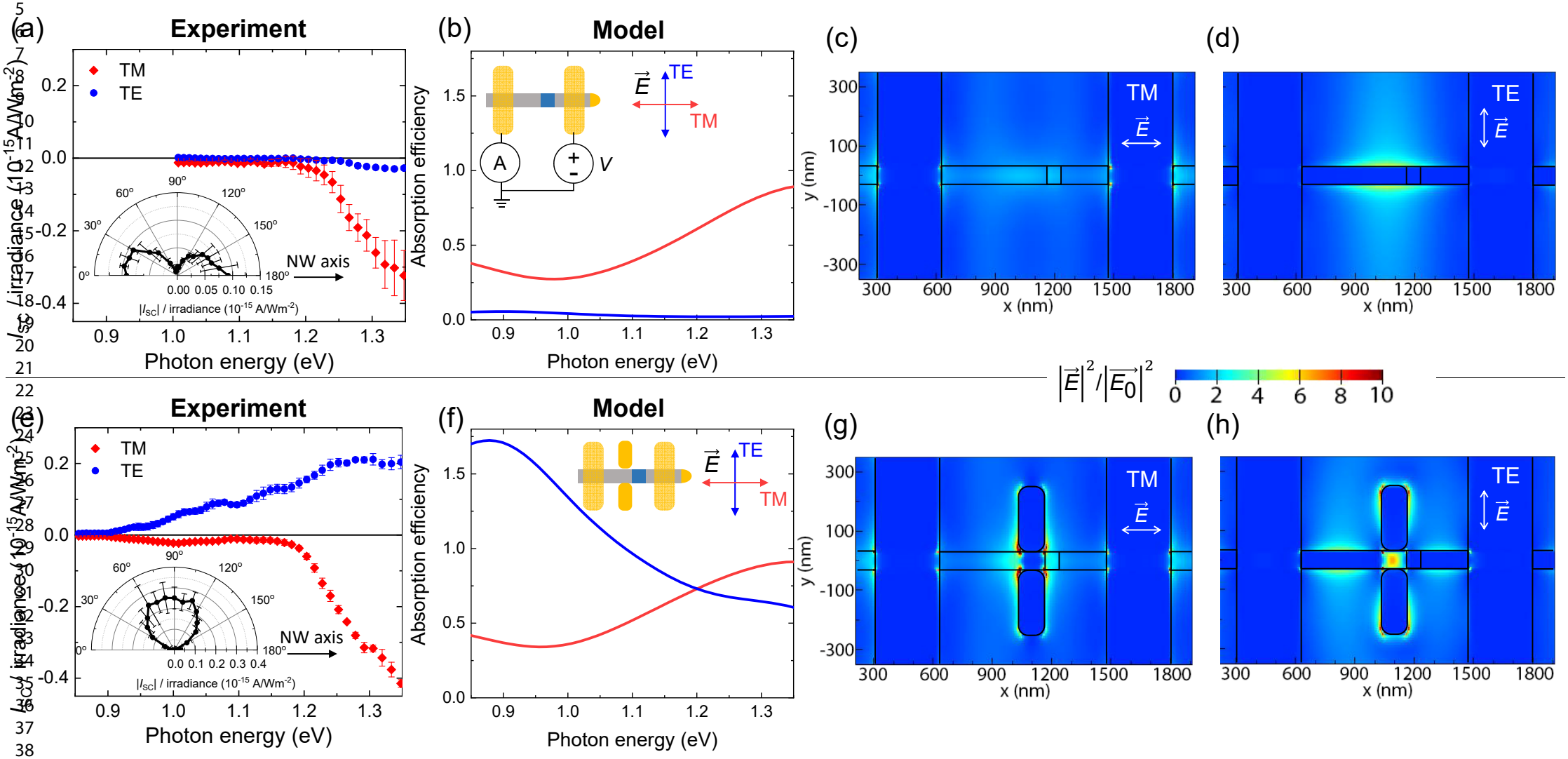
(a)
Experiment
TM
TE
I_{sc} / irradiance (10^{-15} A/Wm^{-2})
Photon energy (eV)
NW axis
$|I_{sc}|$ / irradiance (10^{-15} A/Wm^{-2})
(b)
Model
Absorption efficiency
Photon energy (eV)
A
V
TE
TM
(c)
(d)
y (nm)
x (nm)
$|\vec{E}|^2/|\vec{E_0}|^2$
0 2 4 6 8 10
(e)
Experiment
TM
TE
I_{sc} / irradiance (10^{-15} A/Wm^{-2})
Photon energy (eV)
NW axis
$|I_{sc}|$ / irradiance (10^{-15} A/Wm^{-2})
(f)
Model
Absorption efficiency
Photon energy (eV)
TE
TM
(g)
(h)
y (nm)
x (nm)

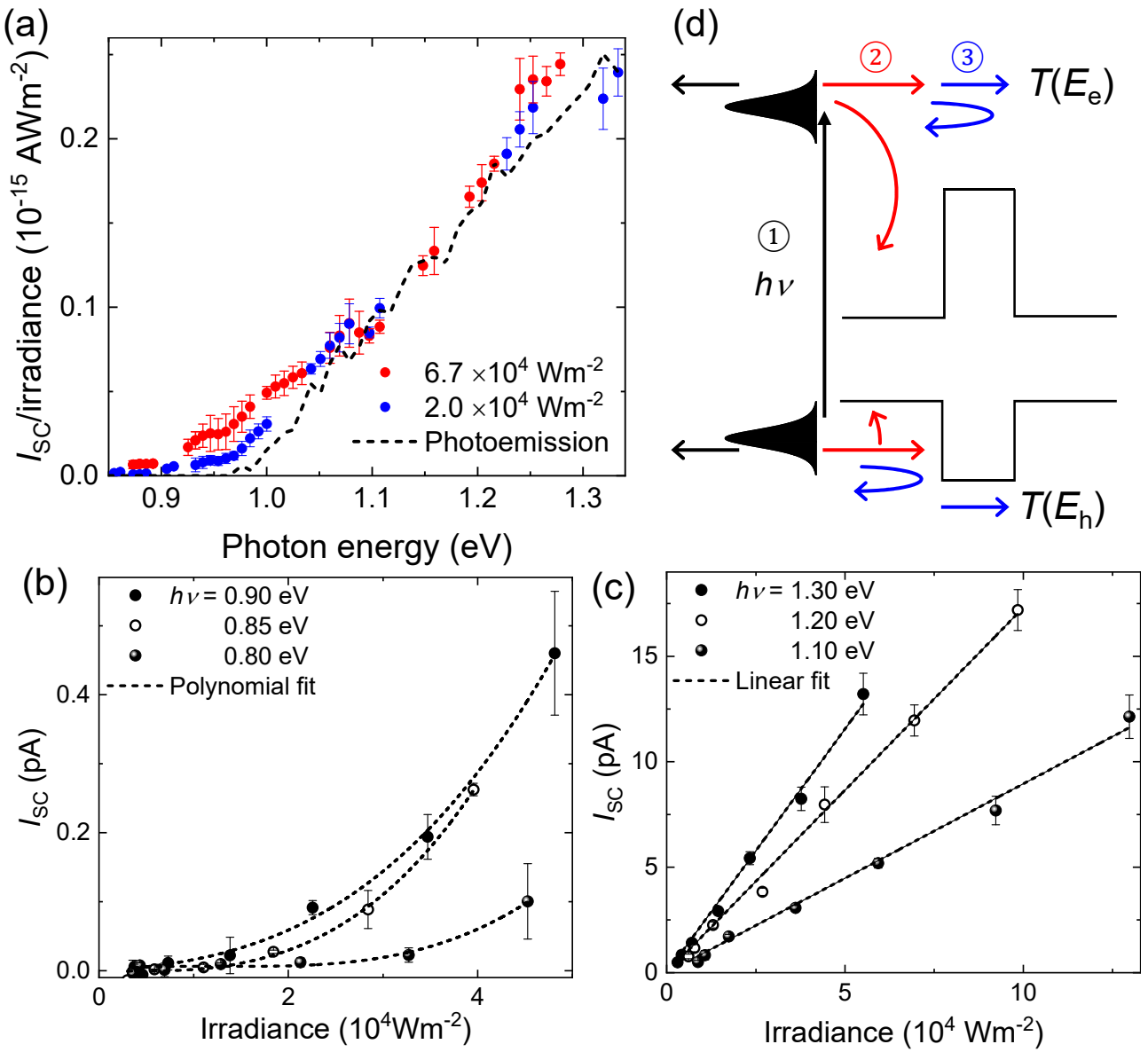
(a)
I_{SC}/irradiance (10^{-15} AWm^{-2})
0.0
0.1
0.2
0.9
1.0
1.1
1.2
1.3
Photon energy (eV)
6.7 ×10^4 Wm^{-2}
2.0 ×10^4 Wm^{-2}
Photoemission
(d)
②
③
$T(E_e)$
①
$h\nu$
$T(E_h)$
(b)
$h\nu$ = 0.90 eV
0.85 eV
0.80 eV
Polynomial fit
I_{SC} (pA)
0.0
0.2
0.4
0
2
4
Irradiance (10^4Wm^{-2})
(c)
$h\nu$ = 1.30 eV
1.20 eV
1.10 eV
Linear fit
I_{SC} (pA)
0
5
10
15
0
5
10
Irradiance (10^4 Wm^{-2})

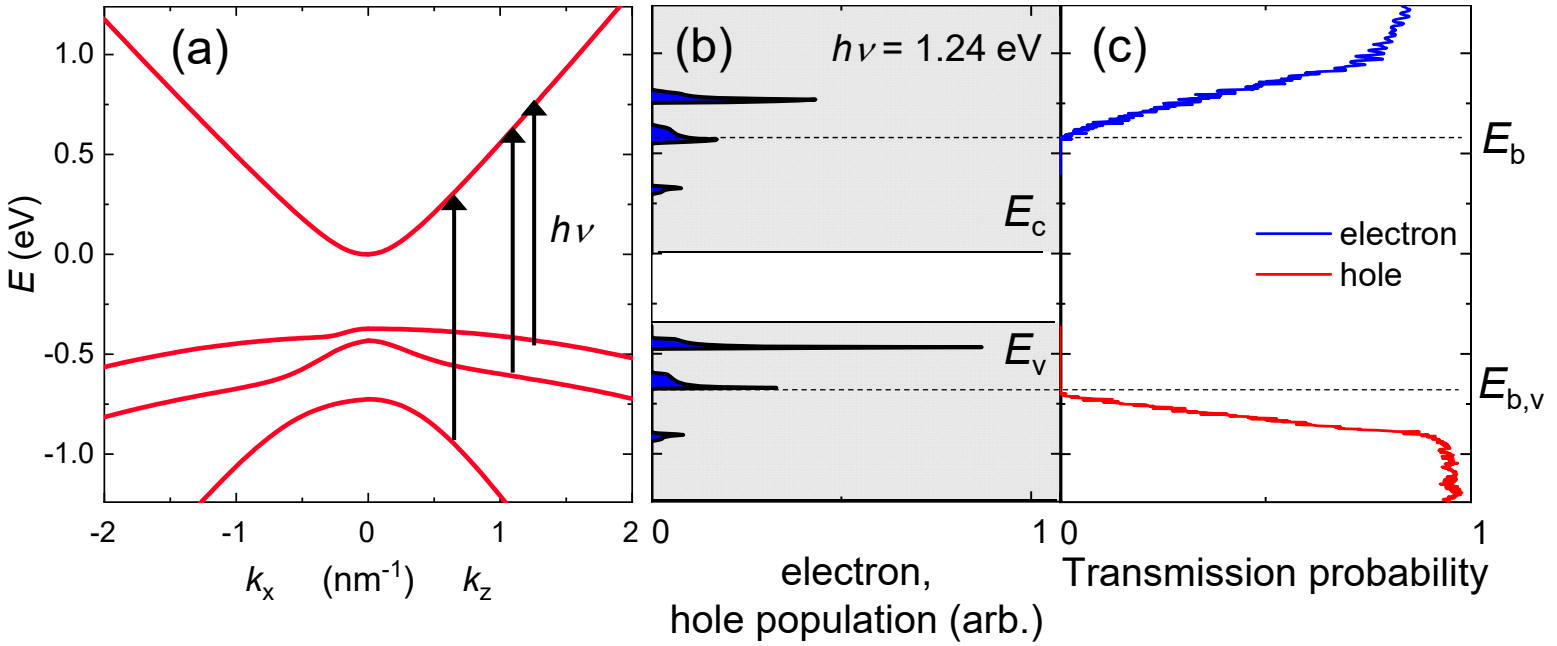
(a)
(b)
(c)
$h\nu$ = 1.24 eV
$h\nu$
E (eV)
1.0
0.5
0.0
-0.5
-1.0
-2
-1
0
1
2
k_x (nm^{-1}) k_z
E_c
E_v
0
1
electron,
hole population (arb.)
E_b
$E_{b,v}$
electron
hole
0
1
Transmission probability

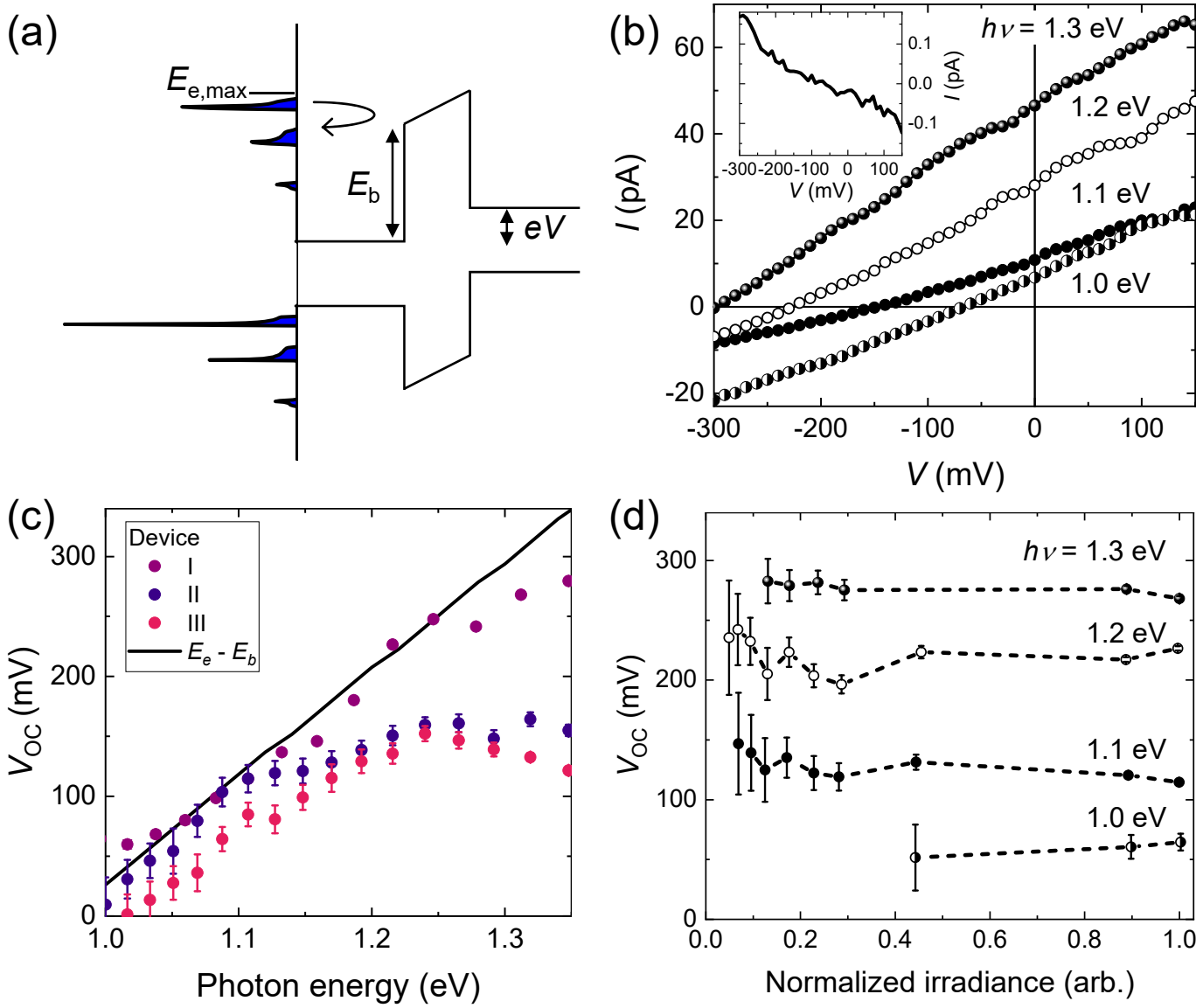
(a)
$E_{e,max}$
E_b
eV
(b)
$h\nu$ = 1.3 eV
1.2 eV
1.1 eV
1.0 eV
I (pA)
V (mV)
(c)
Device
I
II
III
E_e - E_b
V_{OC} (mV)
Photon energy (eV)
(d)
$h\nu$ = 1.3 eV
1.2 eV
1.1 eV
1.0 eV
V_{OC} (mV)
Normalized irradiance (arb.)

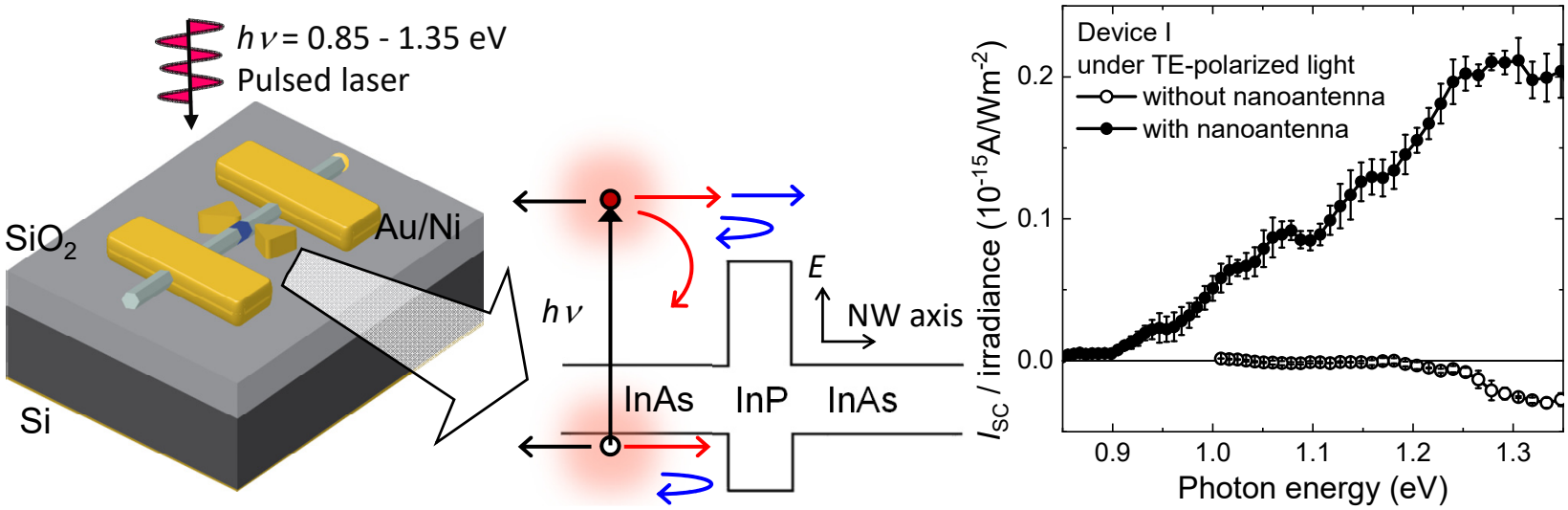
hν = 0.85 - 1.35 eV
Pulsed laser
SiO2
Au/Ni
Si
hν
E
NW axis
InAs
InP
InAs
Device I
under TE-polarized light
without nanoantenna
with nanoantenna
ISC / irradiance (10-15A/Wm-2)
0.2
0.1
0.0
0.9
1.0
1.1
1.2
1.3
Photon energy (eV)